Anisotropic structure-property relations of FDM printed short glass fiber reinforced polyamide TPMS structures under quasi-static compression

Prince Jeya Lal Lazar [a], *Jeyanthi Subramanian* [b], *Elango Natarajan* [c,d,*], *Kalaimani Markandan* [c], *S. Ramesh* [e]

[a] *Department of Mechanical Engineering, Rajalakshmi Institute of Technology, Chennai 600124, Tamil Nadu, India*
[b] *School of Mechanical Engineering, VIT Chennai Campus, Chennai 600127, Tamil Nadu, India*
[c] *Faculty of Engineering, Technology and Built Environment, UCSI University, Kuala Lumpur, Malaysia*
[d] *Department of Mechanical Engineering, PSG Institute of Technology and Applied Research, Coimbatore 641062, Tamil Nadu, India*
[e] *Department of Mechanical Engineering, Jerusalem College of Engineering, Chennai 600100, Tamil Nadu, India*

ABSTRACT

Triply minimal surface structures of short glass fiber reinforced polyamide with different relative densities were prepared and the effects of induced anisotropy, cell topology, and relative density on the compressive properties were evaluated. Schwarz Diamond, Schoen Gyroid, and Schwarz Primitive structures were 3D printed with relative densities ranging from 0.2 to 0.4, and compression properties along the axial and lateral build directions were determined. Gipson-Ashby numerical parameters required to establish a relation between the cell topology and the compressive properties of the lattice structures were estimated. The plastic deformation and failure mechanisms were analyzed. Results revealed that the compression properties are dominated by the cell topology rather than the relative density. Besides, the present work confirmed that the compressive properties of the lattice structures fabricated with short fiber reinforcement are significantly affected by anisotropy. These structures exhibited a higher compressive modulus and lower peak compressive stress in the lateral direction, which can be attributed to the inline orientation of the short glass fibers. Schwarz Diamond proved to be the stiffest structure, followed by Schoen Gyroid and Schwarz Primitive under axial and lateral compression. Likewise, Schwarz Primitive generated low stresses compared to Schoen Gyroid and Schwarz Diamond. All cell topologies deformed in a controlled manner layer by layer, minimizing undulations in the load-bearing capacity of the structures. D and G structures compressed in the axial direction exhibited significant strain hardening and identical structures compressed in the lateral direction exhibited stable post-yield behavior with negligible undulations which is highly preferred for crashworthiness applications.

© 2023 The Authors. Published by Elsevier B.V. This is an open access article under the CC BY-NC-ND license (http://creativecommons.org/licenses/by-nc-nd/4.0/).

1.   Introduction

Structural configurations with high porosity are termed cellular structures and are preferred for a variety of engineering, medical, and sports applications [1–5]. Fabrication of such porous and functional components, which have a considerable degree of manufacturing complexity due to the intricate cellular morphology, is now possible thanks to advanced manufacturing technologies [6,7]. Additive manufacturing is a transformative technology that can eliminate design constraints in the development of cellular structures [8] and enable better manufacturability in the development of multifunctional, architectural, highly porous cellular structures [9,10]. Fused deposition modeling (FDM) [11], poly jet [12], selective laser sintering (SLS) [13], binder jetting [14], projection micro-stereolithography (PμSL) [15], and laser powder bed fusion (LPBF) [16,17] are widely used additive manufacturing techniques for fabricating lattice structures from polymers and metals. Shape memory polymers [18], poly lactic acid (PLA) [19], acrylonitrile butadiene styrene (ABS) [20], polyamide (PA) [13], photosensitive resin [15], bio-polyester [21], nylon PA 2200 [22], polyether-etherketone (PEEK) [23], polyethylene terephthalate glycol (PETG) [24], and thermoplastic polyurethanes (TPU) [25] are widely used polymers for developing lattice structures with high porosity and metallic materials such as steel, inconel, copper, aluminium and titanium alloys [16,26–28] and ceramics [29,30] are widely used materials to manufacture lattice structures through laser additive manufacturing process.

The triply minimal surface structure (TPMS) is a class of lattice designs that offers multifunctional capabilities [31]. It has attracted the attention of researchers in recent years to evaluate the properties of different types of lattice designs with different relative densities since the structural configuration control the failure modes [32] in either a bending-dominated mode or a stretching-dominated mode. The use of strut-based cellular structures has been investigated by researchers [16,33] to design open cell configurations with desirable mechanical properties, as nodal connections can lead to stretch-dominated failure [4]. Strut-based cell configurations exhibit shear deformation bands, usually formed by the rapid failure of struts in successive layers, where the peak stress increases significantly and then decrease rapidly [34], leading to undulations in the load-carrying capacity of the structure due to the orientation of the struts in the loading direction, resulting in a higher elastic modulus. The unevenness in load-bearing capacity and energy absorption can be eliminated by using sheet-based TPMS configurations. Moreover, the mechanical compressive performance of TPMS configurations is highly desirable compared to strut-based configurations with high nodal connectivity [16,35]. The key reason for this is the continuous surface curvature and connectivity, which leads to improved load distribution and bearing capability, thus mitigating the occurrence of stress peaks, and ensuring a smooth transition from elastic to plastic deformation regime with stable plateau stress [32]. A review by [7] summarize the design process and methods for developing TPMS-based cellular structures, as well as the relationship between cell topology and material properties of various TPMS-based configurations. In [36], structure-property correlations of primitives, gyroids, diamonds, and I-WP surfaces of higher relative densities (up to 68%) are clearly elaborated and future directions for the design of scaffold architectures are proposed. In a similar study [13] clarified the deformation patterns and determined the numerical parameters required to establish the relationships between the lattice design and the mechanical properties of primitive, gyroid, and diamond structures. [16] investigated the topology-property relationships of strut, skeleton, and sheet TPMS cell structures and summarized the results to show that sheet-based TPMS configurations followed a stretch-dominated deformation, while skeleton-based TPMS configurations followed a bend-dominated deformation, and the strut-based topologies exhibited a mixed deformation mode. In [12], stress concentration effects are reported to occur in TPMS based frameworks due to a heterogeneous mass distribution at lower volume fractions. Numerical analysis by [37] showed that the thickness and the number of cells in a lattice structure strongly affect the strength, stiffness, and failure pattern. This is due to localized fracture [38], which can be avoided by reducing the size of the unit cells and by choosing an appropriate cell topology.

Although complex lattice designs can be realized through additive manufacturing, the process itself leads to anisotropy in the lattice structures. This leads to the degradation of mechanical properties [39], which can be predicted by the method proposed by [40]. A few studies on FDM-printed strut-based lattice structures [41,42] showed that the mechanical properties and deformation mechanisms are significantly altered by the loading direction and suggested that, in addition to the cell topology, the anisotropy induced by the fabrication process is also a potential factor to be considered in the development and application of such structures. A similar study by [43] investigated the effects of loading direction on the mechanical properties of various TPMS scaffolds developed using FDM. This study confirmed the effects of anisotropy, which is an intrinsic feature of FDM, on the structural performance of TPMS scaffolds. Moreover, it was possible to either increase or decrease the degree of anisotropy to develop customized scaffolds.

3D-printed pure polymers are restricted to be used in structural applications due to the deficiency in mechanical properties [44]. The present work encounters the identified gap by manufacturing short glass fiber-reinforced polyamide composites using the FDM process for load-bearing applications. Previous research on the influence of short glass reinforcement in 3D printed materials like ABS, PLA, PEEK [45–47] reveals that significant enhancement in strength and stiffness could be achieved by compromising ductility. The earlier research is aimed at evaluating the tensile and flexural properties of short glass fiber-reinforced 3D printed polymers and no attention has been paid to the mechanical properties under axial and lateral compression. Although literature [48,54] explores the compression properties of FDM printed short glass fiber reinforced polyamide solid parts, the compression properties of short glass fiber reinforced polyamide porous structures have not been explored so far. Hence, the present work is focused on developing bioinspired lattice structures with minimal surface area and accessing the load-bearing

properties by conducting axial compression experiments at a quasi-static strain rate as the fiber reinforcement exhibits sensitivity to strain rate [48]. Literature [49] reveals that short fiber reinforcement could significantly improve the load-bearing properties of 3D-printed structures. In addition, structures with tailored stiff and ductile properties could be obtained for load-bearing applications [50]. Reinforcement with short carbon fibers resulted in significant improvement in tensile strength and modulus of the 3D-printed ABS specimens in the order of ~115% and ~700%, respectively. A similar study [51] reported a sevenfold increase in tensile modulus and a twofold increase in strength by reinforcing 35 wt% chopped carbon fibers with PA12. The effect of short carbon reinforcement material in ABS, scan strategy, printing temperature, scan angle, and the effects of short glass fiber reinforcement in PA are presented in [52−54].

Although there are very little literature on the processing parameters and manufacturability of short glass and carbon fiber reinforced polyamide composite blocks using FDM [48,54], to the best of the author's knowledge, no attempt has been made to develop short glass fiber reinforced sheet-based minimal surfaces using FDM process. Considering the significant influence of anisotropy on mechanical properties, it is very much essential to evaluate the structure-property relationships of short glass fiber-reinforced sheet-based structures subjected to axial and lateral compression. Failing to, it limits the use of these structures for engineering applications. This research, therefore, attempts to fill these gaps by developing ePA-GF TPMS lattice structures with different relative densities and establishing their relationship to structural configurations and properties.

2. Methodologies

2.1. Design of TPMS structures

To choose the appropriate lattice configuration for a material with a plastic yield point [55] proposed the following power law for assigning the exact volume fraction or relative density.

$$\phi_L = C \, \phi_S \, \rho^{*n} \qquad \text{(i)}$$

where ϕ_L is the mechanical property of the lattice, ϕ_S is the mechanical property of the principal material, and C is a geometric proportionality constant to account for the imperfections in the structures. The geometric factor with $C = 1$ represents an ideal defect-free 3D printed lattice structure, while values of $C < 1$ indicate imperfections in the printed lattice depending on the applied load, cell topology, and boundary conditions, where ρ^* is the relative density ($\rho^* = \rho_L/\rho_S$, ρ_L - density of printed lattice, ρ_S - density of bulk material) and n is the scaling exponent that phenomenologically describes the deformation mechanisms as stretching ($n = 1$) or bending ($n = 2$), while other values of n indicate mixed deformation [22]. Typical values of n can be estimated by manufacturing lattice structures with different relative densities followed by fitting the experimental data [56,57]. Variation in the elastic modulus and plateau stress is witnessed in lattice structures for varying cell topology with equivalent relative density.

The current research deals with triply minimal surfaces (TPMS), which are bioinspired, edge-free, and non-self-intersecting continuous surfaces with zero mean curvature at all points on the sheet surface and divide 3D space into two regions [37,58]. TPMS structures are generated by level-set surface equations [59] of form f (x, y, z) = c, where a single unit cell (x, y, z) is bounded by (0, 2π) and c is the level-set parameter. The relative density of the structures can only be controlled by assigning a thickness of -c $\leq$ f $\leq$ c to the surfaces for the equivalent unit cell size. Therefore, the lowest relative density is limited based on the minimum printable surface thickness because it is difficult to print TPMS structures with a smaller unit cell size or a lower relative density [60]. In this work, three different TPMS configurations with different relative densities in the order of 0.29, 0.32, and 0.39 derived based on the minimum printable sheet thickness are built using the following approximations presented in [61].

Schwarz Diamond [D]:

$$\sin(x)\sin(y)\sin(z) + \sin(x)\cos(y)\cos(z) + \cos(x)\sin(y)\cos(z) + \cos(x)\cos(y)\sin(z) = 0 \text{ eq.} \qquad \text{(ii)}$$

Schoen Gyroid [G]: $\cos(x)\sin(y) + \cos(y)\sin(z) + \cos(z)\sin(x) = 0$ eq. (iii)

Schwarz Primitive [P]: $\cos(x) + \cos(y) + \cos(z) = 0$ eq. (iv)

TPMS structures with smaller unit cells and lower thickness are very difficult to print [60] and from the results of [62], it is understood that the size of the unit cell of the cellular structures affects the mechanical properties. Therefore, the lattice structure is designed with a 5*5*5 periodicity with a unit cell size of 8 mm as recommended by [13,63]. For a fixed unit cell size of 8 mm, the variations in the relative density of the lattice structures are attained by assigning thickness to the lattice surface. This increases the lattice volume which is directly proportional to the relative density of the lattice. For instance, the volume of a unit cell is increased to 151.59 mm^3, 166.44 mm^3, and 200.94 mm^3 for the thickness of 1.02 mm, 1.12 mm, and 1.35 mm respectively in the D structure. Similarly, the sheet thickness of G and P structures are varied by trial and error to attain equivalent relative densities. The CAD models of the unit cells with different relative densities of the different TPMS configurations are presented in Fig. 1.

2.2. FDM printing of TPMS lattice structures

Fused deposition modeling (FDM) is used to develop the TPMS lattices for this study. This is an ASTM 52900 material extrusion process in which molten polymer is selectively deposited layer by layer through a heated nozzle based on CAD data [64]. The filament consists of ePA-GF (manufacturer: Shenzhen Esun Industrial Co., Ltd., China), a nylon 6/66 copolymer reinforced with short glass fibers used to fabricate the lattice structures. ePA-GF is formulated to be stiff and strong without being brittle, with improved mechanical properties compared to pure nylon. In addition, the ePA-GF filaments offer excellent printing performance with minimal edge deformation, shrinkage, and distortion. The physical, mechanical, and thermal properties of ePA-GF are listed in Table 1.
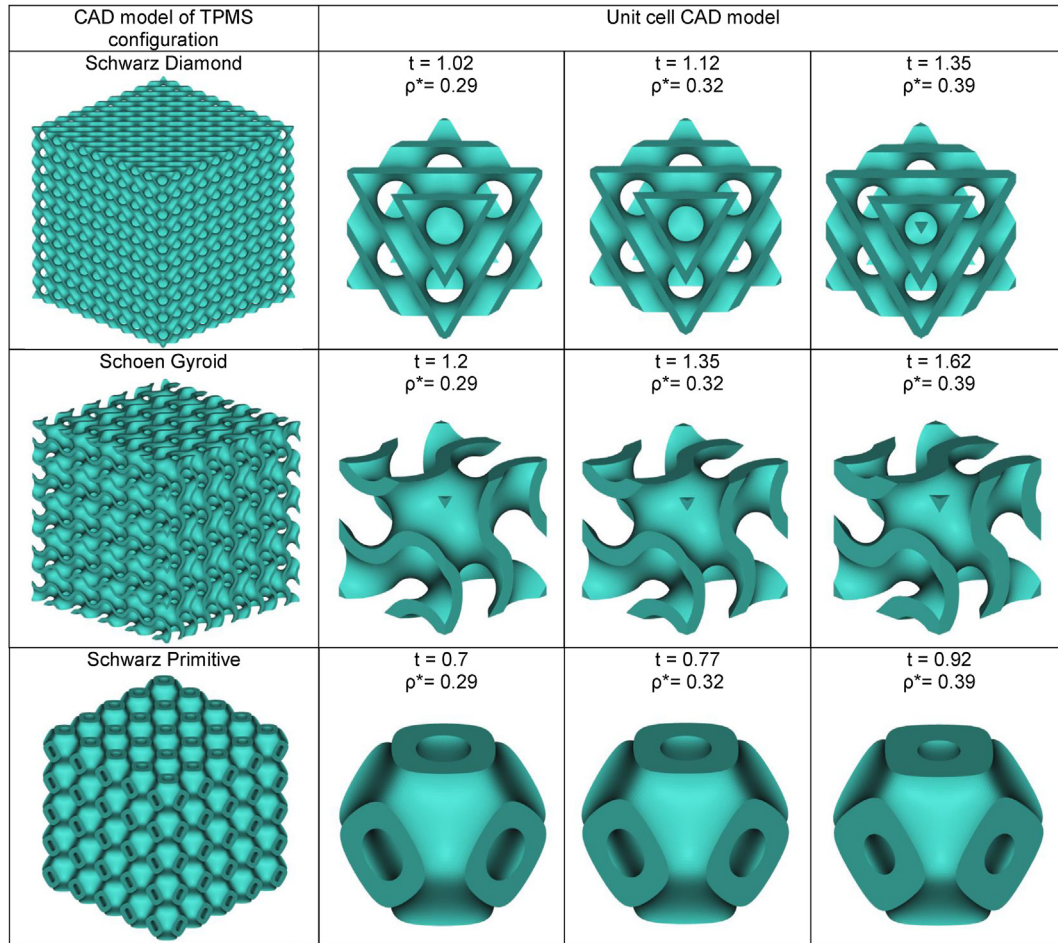
CAD model of TPMS configuration	Unit cell CAD model		
Schwarz Diamond	t = 1.02 ρ*= 0.29	t = 1.12 ρ*= 0.32	t = 1.35 ρ*= 0.39
Schoen Gyroid	t = 1.2 ρ*= 0.29	t = 1.35 ρ*= 0.32	t = 1.62 ρ*= 0.39
Schwarz Primitive	t = 0.7 ρ*= 0.29	t = 0.77 ρ*= 0.32	t = 0.92 ρ*= 0.39

Fig. 1 — CAD Models of TPMS configurations and unit cells with different sheet thicknesses and relative densities.

Printing of all TPMS structures uses an in-house developed 3D printer with a two-fan configuration with controllable speed for improved print quality and sophisticated extruder sensors for accurate leveling to improve dimensional accuracy. Since reinforcing fiberglass additives clog the nozzle more frequently, a stainless-steel nozzle with slow speed and reduced retraction greatly improve extrusion quality. It is recommended to dry the filaments in the oven at 70 °C for 3—4 h before starting the printing process to mitigate the effects of moisture. In addition, the tool path generated in the pre-processing phase has a significant impact on the printing process and results [66], ultimately leading to parts with poor mechanical properties. Therefore, proper planning of the tool path is very important to achieve optimal dimensional accuracy, printing time, material consumption, and print quality [67]. A suboptimal tool path limits the printing of micro-geometric features, resulting in unrepresented edges and voids due to abrupt changes in tool motion in TPMS structures [68]. In this study, an open-source slicing application CURA from Ultimaker is used in the pre-printing phase to prepare the model for FDM printing. The recommended

Table 1 — Physical, mechanical, and thermal properties of ePA-GF according to manufacturer's specifications [65].

Properties	Value
Filament color	Beige
Filament Diameter (mm)	1.75
Max. Roundness deviation (mm)	±0.05
Mechanical Properties	
Density (g/cm^3)	1.35
Tensile strength at yield (MPa)	76.93
Tensile Modulus (MPa)	3953
Elongation at break (%)	21.07
Impact strength (Izod-notched) (kJ/m^2)	14.65
Flexural strength (MPa)	77.75
Flexural modulus (MPa)	1714.63
Thermal properties	
Melt mass-flow rate (MFR) (g/10 min)	15
Distortion temperature (°C, 0.45/MPa)	120.7
Thermal expansion coefficient (/K)	0.1x10-4
Others	
Glass fiber content (%)	25
Moisture absorption, 24h (%)	0.7—1.1

Table 2 — Recommended FDM printing parameters for ePA-GF.

Process parameter	Value
Nozzle diameter (mm)	0.4—0.6
Nozzle distance (mm)	0.2—0.3
Nozzle temperature (C)	240—260
Bed temperature (C)	60—90
Chamber temperature (C)	80
Layer height (mm)	0.12
Infill density (%)	100
Infill pattern	Triangle
Infill speed (mm/s)	60—90
Print Speed (mm/s)	90—150
Cooling fan	off
Build plate adhesion type	Raft

printing parameters are listed in Table 2. In addition, the processing and manufacturability of the fiber-reinforced composites by FDM must be well understood because the scanning strategy combined with the printing temperature significantly affects the elastic modulus and yield strength due to the significant anisotropy induced by the orientation of the short fibers [54].

2.3. Quasi-static compression experiments

The structure-property relationships that exist in the ePA-GF TPMS structures developed using the FDM technique are evaluated through the experimental compression behavior of the structures. The compression properties of the TPMS structures are investigated by uniaxial compression experiments referring to ISO 13314:2011 using an Autograph AGS-X series universal testing machine (manufacturer: Shimadzu Corporation, Japan) in displacement-controlled mode with a strain rate of 0.001 s^{-1} and a load cell of 50 kN capacity. The specimens are placed exactly in the center of the steel compression plates to avoid misalignment. Three repetitions for a sample in the initial study revealed that the deviations in compression properties are less than 6%. This repeatability is due to the optimized printing parameters and the microvoids had no significant influence on the compression properties. For further experiments, one sample is compressed and the results are tabulated. The compressive force applied to the specimens is measured and the corresponding displacement is recorded until the TPMS structures are compacted. The whole experiment was recorded with a high-resolution video camera, which is used to study the progressive collapse
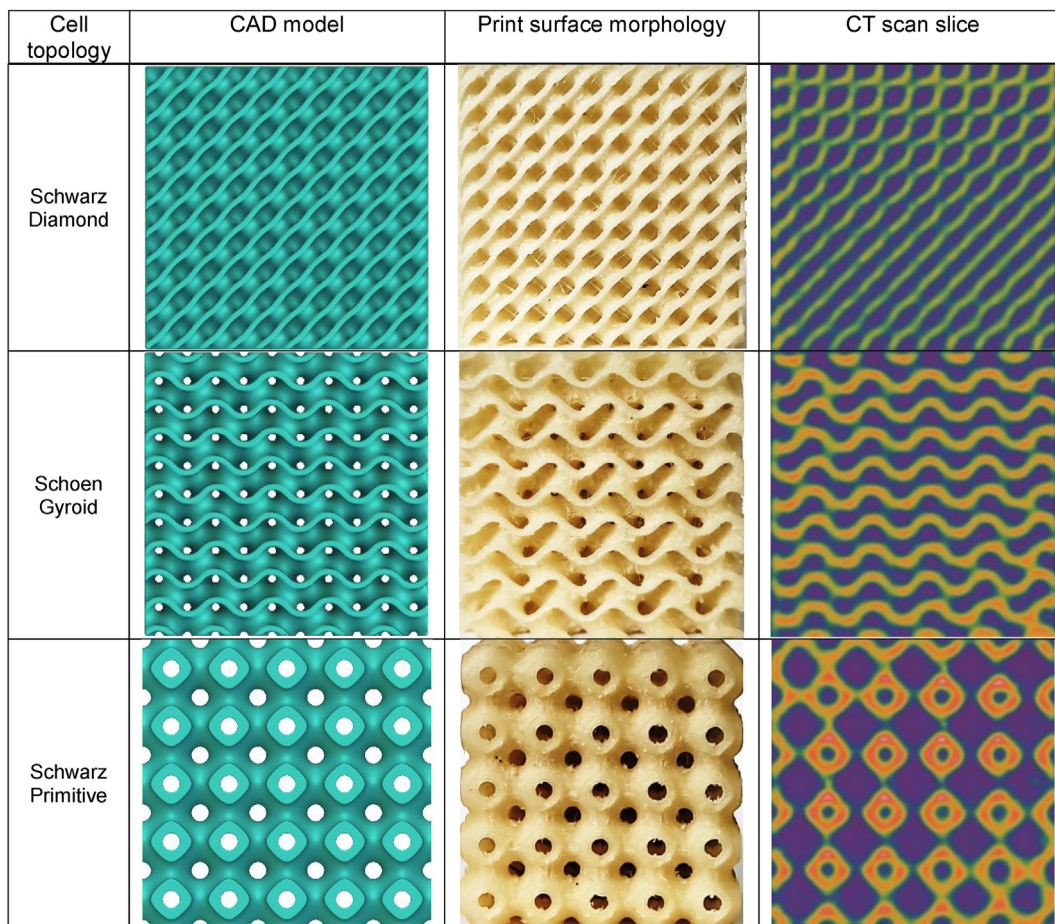

Fig. 2 — Comparative view of printed parts: CAD design model representing the build FDM prints with corresponding CT slice image.
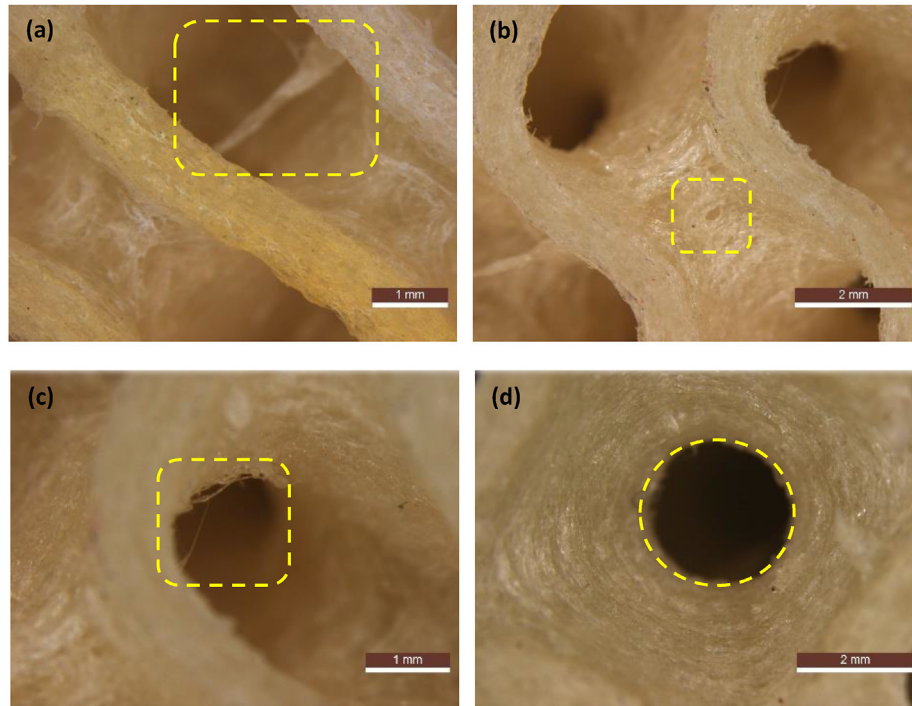
Fig. 3 — Surface defects of ePA- GF TPMS structures printed with FDM imaged through an optical microscope (a) cell bridging in D structures (b) & (c) pores and stringing in G structures (d) geometry defects in P structure.

behavior of the TPMS structures. The compression modulus is determined from the linear region of the stress-strain curve, and the peak compressive stress is the highest stress induced in the structure between the first peak stress and the onset of compression. The specific energy absorption is determined from the stress-strain curves using eq. (v). While the onset of densification is often referred to as densification strain in the literature, which is not accurate, it can be evaluated by at least four different techniques, which are (i) by a point corresponding to the maximum efficiency, (ii) by a predefined strain value, which is typically 40% or 50%, (iii) by using the first peak compressive stress as a threshold, and (iv) by the intersection of the slope developed from the plateau and densification regimes [69–72]. In this work, the strain corresponding to the maximum efficiency is considered the onset of densification. The failure mechanisms of the ePA-GF structures are understood by examining the fractured structures with the S–3400 N (manufacturer: Hitachi, Japan) scanning electron microscope.

$$SEA = \frac{\int_0^{\varepsilon_d} \sigma \, d\varepsilon}{\rho_L} \qquad (v)$$

where ε_d is the strain corresponding to the onset of densification and ρ_L is the density of the printed lattice.

3. Results and discussion

3.1. Print quality assessment

Before experimental testing, all 3D-printed TPMS structures are analyzed for print quality and dimensional accuracy using the Leica M205C stereo microscope, which can achieve an optical resolution of 0.952 μm. In addition, the internal quality of the prints is analyzed using a GE LightSpeed VCT CT scanner with SnapShot Pulse™ interface, operating at 200–500 mA. The relative densities of all TPMS structures are measured as described in [73]. Figs. 2 and 3 show the print quality, internal morphologies, and defects observed in the TPMS structures (see Fig. 3).

All 3D printed TPMS structures are very consistent with their 3D CAD models and no significant macro defects such as distortions or loss of cell junctions were detected. In addition, the CT images show smooth transitions that are characteristic of TPMS. Both the optical and CT cross-sectional images show satisfactory print quality and manufacturability for all TPMS configurations. It can also be observed that the deviations are higher for TPMS structures with a higher degree of complexity. For example, the maximum deviation is 4.63% for Schwarz Diamond, 9.85% for Schoen Gyroid, and 12.93% for Schwarz Primitive. In general, it can be observed that for Schwarz Diamond and Schoen Gyroid TPMS structures, the deviation of the design mass from the printed mass shows a decreasing trend with increasing sheet thickness, which is attributed to the printability of the selected TPMS structure. These deviations are due to the printability of the design wall thickness and the complex surface geometry of the TPMS structures. For example, the calculated surface area for the three cell configurations with a fixed design RD of 0.29 is 63121.7 mm^2, 50116.73 mm^2, and 38252.94 mm^2 for Schwarz Diamond, Schoen Gyroid, and Schwarz Primitive structures, respectively. The relationship between the sheet thickness and relative density is shown in Fig. 4 with the corresponding fitting parameters.
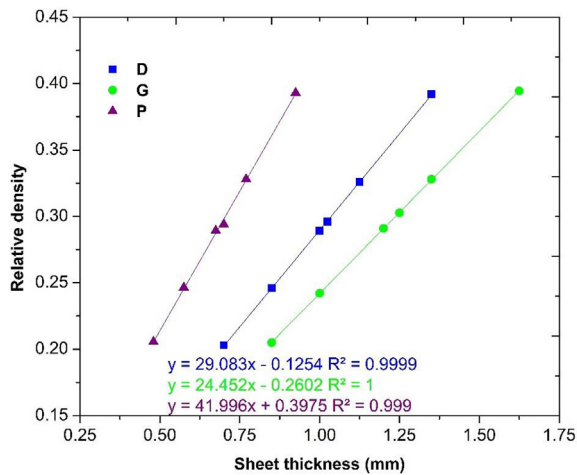
Fig. 4 – Effect of lattice sheet thickness on relative density with fitting parameters.

For P structures, increasing the sheet thickness from 0.7 mm to 0.77 mm and 0.92 mm increased RD by 11.5% and 33.6%, respectively. A similar trend was observed for the D and G structures. CT Scan slices in Fig. 2 are shown for a better understanding of the internal morphology, which has no defects due to layer interruptions, as developed in [62]. The printed properties of TPMS structures are shown in Table 3.

3.2. Experimental response

To understand the anisotropic properties, all 18 printed structures were tested under compressive loading in the axial and lateral directions since the loading direction can significantly affect the properties of short fiber-reinforced FDM parts [74]. The plotted stress-strain curves of a cell topology for different levels of relative densities for all structures are

shown in Fig. 5. The vertical lines represent the onset of densification. An increase in mechanical properties with increasing relative density is observed for all tested specimens, and structures with similar topologies showed comparable responses. However, structures with similar topologies showed different responses when tested laterally and axially.

3.2.1. Axial compression response
The recorded stress-strain curves of all 9 structures compressed in the axial direction are shown in Fig. 5(a–c). The stress-strain curves of all D, G, and P structures showed a typical observation with an initial linear phase for strains $\varepsilon <$ 5% and immediately followed by a plateau region with no clear yield point until the onset of densification. Although the plateau region appeared to be smooth and without undulations in all structures (except P1 and P2), significant hardening due to bulk properties and self-contact was observed until the onset of densification as the slope of the plateau region showed an increase with the relative density of the structures. Over time, after all cells were confined, and beyond the onset of densification, a steep increase in stress was observed. The P1 and P2 structures exhibited a different pattern with slight softening and hardening, respectively, with negligible plateau slope and were free of undulations. However, the carbon fiber-reinforced PLA structures with similar relative density and larger cells exhibited severe softening in D and P structures and severe undulations in P structures [69]. Under axial compression, debonding at the interfaces of successive cell layers resulted in increased strain due to poor bonding and voids. This resulted in a delay in the onset of densification. In this study, all structures reached the onset of densification within 55–60% of the strain.

3.2.2. Lateral compression response
The plotted stress-strain curves of all 9 structures compressed in the lateral direction, Fig. 5. (d - f), show a characteristic

Table 3 – Measured properties of the printed TPMS structures.

Test Order	Cell Topology	Structure ID	RD	Mass (g)	Deviation (%)
1	Schwarz Diamond	D1A	0.29	24.84	0.95
2		D1L	0.29	24.34	−0.51
3		D2A	0.34	26.4	4.63
4		D2L	0.32	25.28	0.34
5		D3A	0.4	31.12	3.31
6		D3L	0.38	29.75	−1.45
7	Schoen Gyroid	G1A	0.28	22.5	−4.35
8		G1L	0.28	22.54	−4.18
9		G2A	0.32	26.34	0.00
10		G2L	0.31	25.55	−2.65
11		G3A	0.42	30.52	7.12
12		G3L	0.43	30.95	9.85
13	Schwarz Primitive	P1A	0.28	22.34	−4.42
14		P1L	0.27	21.77	−6.33
15		P2A	0.32	25.12	0.18
16		P2L	0.36	28.00	11.68
17		P3A	0.43	29.72	11.32
18		P3L	0.44	30.11	12.93

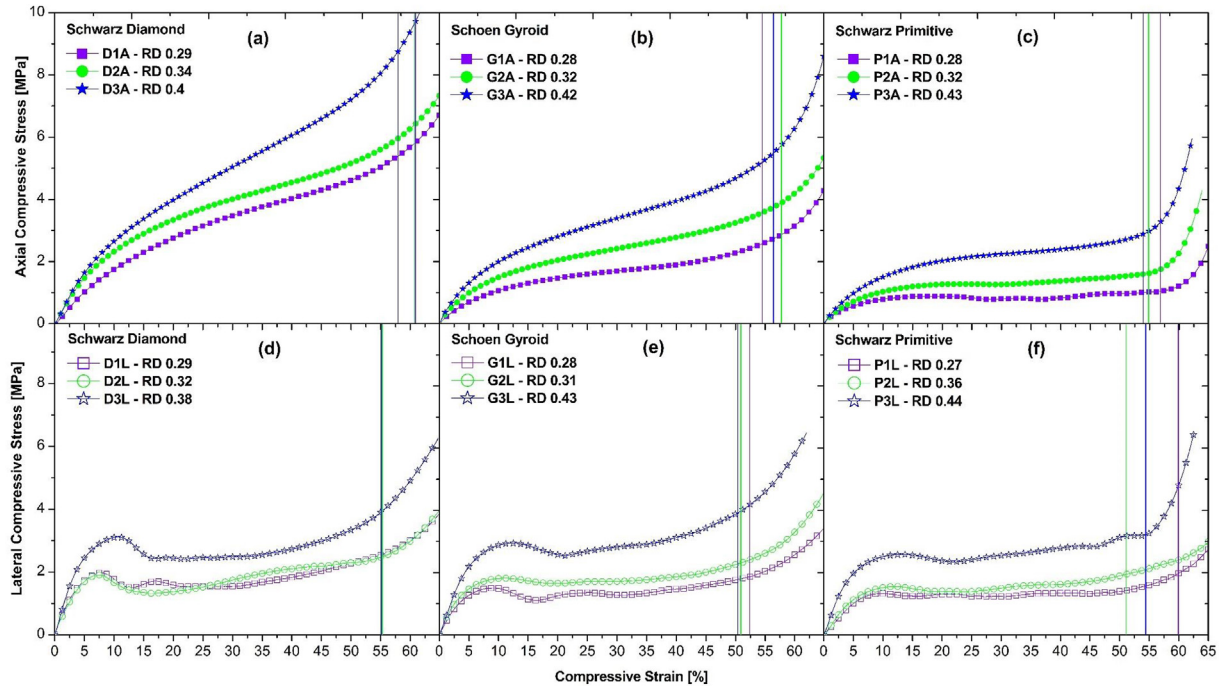*Text A & L in structure ID represent the structure is compressed under axial and lateral directions.

Fig. 5 — Compression responses of lattice structures under (a—c) - axial compression (d—f) - lateral compression, a & d - D structure, b & e — G structure, c & f - P structure.

stretch-dominated curve with four distinct phases; (i) A linear phase up to which a linear increase in the associated stress is observed with the applied strain, from which the modulus of elasticity is estimated from the slope (0 < ε < 5%). (ii) The second phase is referred as the nonlinear phase because the stress-strain curve begins to deviate from the linear response and continues until it reaches the first stress maximum, represented by a peak, after which there is a drop in the curve due to the development and propagation of failure mechanisms in the structures. (iii) The plateau phase is a progressive collapse phase in which the polymer structure follows certain failure mechanisms such as shear bands [75,76] until all cell layers of cells in the structure have deformed, and the end of the phase is identified with the steep increase in stress levels, which represents the onset of densification and can be identified as the peak of the efficiency curve. The deformation patterns in the plateau phase could depend on the cell topology. (iv) The densification phase is the final phase, which represents the complete compression of the structure. With further compression, the stress-strain curve increases dramatically without significance.

It can be observed that the stress-strain curves for a typical cell topology show identical patterns for different relative densities. All D structures exhibited a sharp first peak and then entered the plateau phase. Thereafter, D1L recorded a second peak, D2L exhibited a slight softening, and D3L showed no significant hardening or softening. With continuous compression, all D structures D1L, D2L, and D3L began to harden at 30%, 20%, and 35% strain until compaction began at 55% strain. Similar observations are made for all G-structures, where the structures exhibited a broad first peak and then

shifted to the plateau phase. However, all structures reached the onset of densification earlier than the D structures at 52.5% strain. As for the P structures, P3L exhibited a typical stress-strain curve like D3L and G3L, while P2L exhibited a slight softening and then proceeded with the onset of densification. The compression behavior of P1L was interesting as there was no visible hardening/softening and undulations in the plateau region, which represents a stable failure. In addition, P1L recorded a strain of 60% to reach the onset of the densification limit, which is the highest of all structures compressed in the transverse direction. Typically, all structures developed an initial stress peak within 15% strain, followed by a plateau region due to the collapse of cells along horizontal layers. All structures compressed in the lateral direction exhibited higher stiffness than those compressed in the axial direction, which contradicts the results of [43] where a slight increase was observed due to the absence of reinforcements. In this study, the reinforcing fibers were aligned with the direction of movement of the nozzle during layer deposition and perpendicular to the direction of compression to produce stress peaks during the onset of the plateau phase. These results are identical to the lateral compression behavior of short carbon fiber reinforced polymer TPMS structures presented in [62,77].

3.3. Effects of relative density and cell topology on mechanical properties

In this section, the effects of relative density on the structure-property relationships of the D, G, and P structures under axial and lateral compression are compared in terms of uniaxial

Table 4 – Anisotropic compressive properties of short fiber reinforced TPMS structures.

Test Order	TPMS Topology	Structure ID	Compressive Modulus [MPa]	Peak Compressive Stress [MPa]	Specific Energy Absorption [J/g]	Strain at the onset of densification [%]
1	Schwarz Diamond	D1A	22.82	5.82	5.18	60.9
2		D1L	37.87	2.54	2.51	55.17
3		D2A	32.98	6.39	5.63	60.8
4		D2L	36.59	2.48	2.45	55.27
5		D3A	37.23	8.75	5.73	58.01
6		D3L	57.42	3.43	2.83	51.11
7	Schoen Gyroid	G1A	14.1	2.57	2.41	54.6
8		G1L	28.47	1.86	2.02	52.40
9		G2A	19.94	3.89	3.23	57.8
10		G2L	31.86	2.30	2.18	50.91
11		G3A	26.80	5.49	3.77	56.49
12		G3L	51.96	3.91	2.88	50.40
13	Schwarz Primitive	P1A	11.07	1.03	1.32	56.89
14		P1L	21.21	1.41	1.41	59.94
15		P2A	14.47	1.62	1.69	54.92
16		P2L	27.90	2.39	2.73	51.12
17		P3A	20.38	2.88	2.32	53.99
18		P3L	46.85	3.21	2.89	54.47

compressive modulus, peak stress, and specific energy absorption.

3.3.1. RD vs compressive modulus

From the results presented in Table 4, the D structures have the highest stiffness, followed by the G and P structures, and the same trend was observed in both compression directions. However, it is observed that the stiffness of the structures is significantly higher in lateral compression. Fig. 6 shows the effects of relative density on the modulus of elasticity under

Fig. 6 – Effect of RD on compressive modulus for various cell topologies under axial and lateral compression loading.

axial and lateral compression. With increasing relative density, a steady increase in elastic modulus was observed for all structures under axial and lateral compression. Under axial compression, the D structures exhibited stiffness values of 22.82, 32.98, and 37.23 MPa, respectively. It is obvious that compared to D1A, whose relative density is the lowest in the group, an increase of 44.5% and 63.1% is observed for D2A and D3A. Similarly, the G structures had stiffness values of 14.1, 19.94, and 26.8 MPa, with G2A and G3A showing increases of 41.3 and 89.9% compared to G1A. However, all the G structures had lower stiffness compared to the D structures, in the order of 38.1, 39.5, and 28%. The P structures had stiffness of 11.07, 14.47, and 20.38 MPa, which is on average 24% less than the G structures and 50% less than the D structures.

Under lateral compression, the D structures recorded stiffness values of 37.87, 36.59, and 57.52 MPa. In contrast, G structures had stiffness values of 28.47, 31.86, and 51.96 MPa, and P structures had stiffness values of 21.21, 27.90, and 46.85 MPa. On average, G structures had 16% lower stiffness values compared to D structures whereas, P-structures had 15.9% and 28.7% lower stiffness values compared to G- and D-structures, respectively. The lateral compression results were interesting. The stiffness of all D, G, and P structures increased by 43.7%, 85.1%, and 104.7%. This is due to the plasticity caused by local strain hardening. The values of the exponent n for the D, G, and P structures are 1.54, 1.549, 1.35, and 1.56, 1.44,1.19 for the structures compressed in the axial and lateral directions, respectively, indicating that the structures undergo stretch-dominated deformation. The relative density had no significant effect on the failure patterns, as the deformation was uniformly distributed throughout the structure in layers. However, for D structures, local buckling was observed at strain values of 20%, followed by progressive failure. In general, under compression, cells of D structures established contact with adjacent cell walls due to insufficient space to stimulate cell wall movement, resulting in higher stiffness. Under axial compression, the D-structures reached the onset of densification limits at 60.9, 60.8, and 58.00%
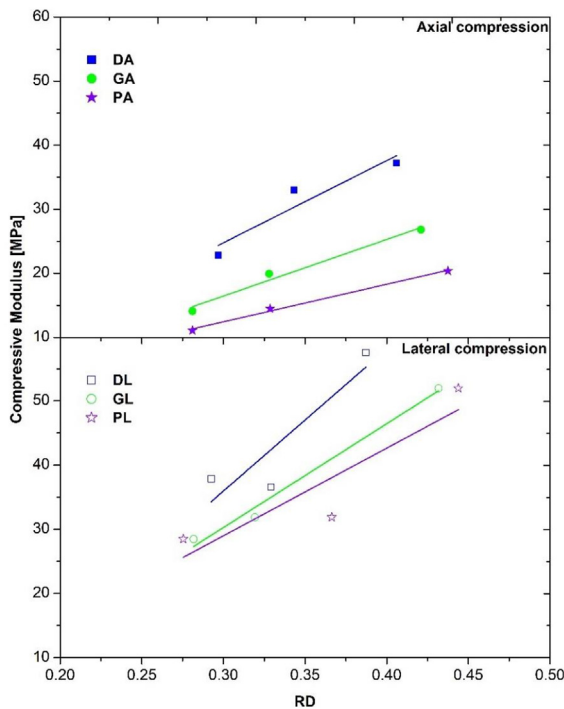
strain, with associated densification stress being 5.82, 6.39, and 8.75 MPa. Under lateral compression, full compression is observed at 55.1, 55.2, and 51.11% strain with 2.54, 2.48, and 3.43 MPa as densification stresses. The G-structures exhibited similar behavior to the D-structures at axial and lateral compression. The densification limit was reached at strains of 54.6, 57.8, and 56.4% during lateral compression, and the densification stresses were reported to be 2.57, 3.89, and 5.49 MPa. During lateral compression, the stresses are 1.86, 2.3, and 3.91 MPa, and the corresponding strains were 52.4, 50.91, and 50.40%. In the axial direction, the P-structures reached full compression at 56.8, 54.9, and 53.9% elongation, respectively, with stresses at the beginning of compression of 1.29, 1.93, and 3.19 MPa. Similarly, the P structures under lateral compression reached the onset of densification limits at 59.9, 51.1, and 54.4% strain. These strains were at stress values of 1.41, 2.39, and 3.21 MPa. Under axial compression loading, P1A maintained a longer plateau range, which was 57% at the lowest compressive stress and 60% in the lateral direction. This is an important performance metric for energy absorption design.

3.3.2. RD vs compressive stress

It is very important to pay attention to the stress peaks induced in structures since high stresses can induce catastrophic failure states that compromise the integrity of the structure. Therefore, from the designer's point of view, a structure with the lowest induced stresses between the first peak and the start of compaction, in combination with other satisfactory characteristics, is preferable. Since the stress at the onset of densification is high, it is referred to as the peak stress in this study. This section summarizes the effects of cell topology and relative density on peak stress derived from the axial and lateral compression experiments. From Fig. 7, for the same cell topology and different relative densities, an increase in peak stress is observed in all structures. Under axial compression, peak stress values of 5.82, 6.39, and 8.75 MPa are obtained in the D structures. Compared to D1A, an increase of 9.8% and 36.7% is observed in D2A and D3A, respectively. Similarly, in the G structures, the peak stress is 2.57, 3.89, and 5.49 MPa for RD with a value of 0.28, 0.32, and 0.42, and compared to G1A, an increase in peak stress on the order of 51.2% and 113.5% is observed, and in the P structures, the induced peak stress is 1.03, 1.62, and 2.8 MPa with an increase of 55.9% and 177.2% compared to P1A.

To understand the general trend of induced peak stress structures, an average reduction of 44% is observed for G structures compared to D structures, and an average reduction of 74.6% and 55.1% is observed for P structures compared to D and G structures. A similar observation was also made under lateral compression as well. The G structure recorded a 6.5% reduction in peak stress compared to the D structure. A reduction of 18% and 12.6% is observed for the P structure compared to the D and G structures, respectively. Compared to axial compression, a 59.4% and 32.28% reduction in peak stress is observed for the D and G structures. The P structures, on the other hand, recorded an average increase of 31.9%. The values of exponent n for D, G, and P structures are 1.31, 1.83, and 2.28 for axial and 1.12, 1.74, and 1.73 for lateral compression.
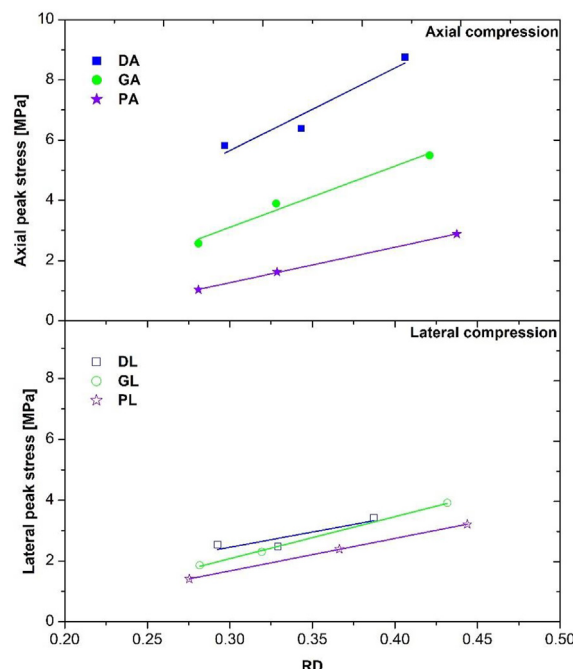

Fig. 7 — Effect of RD on peak compressive stress for various cell topologies under axial and lateral compression loading.

3.3.3. RD vs specific energy absorption

Specific energy absorption, which is the total energy absorption up to the onset of densification normalized to the mass of the structure, plays an important role in understanding the effectiveness of the structure in absorbing energy. An increase in RD would result in enhanced energy absorption with an increase in the associated stress. Thus, an ideal energy absorber must have high specific energy absorption at the lowest stresses, as shown in Fig. 8, which serves as a guide for selecting structures for energy absorption applications while ensuring structural integrity. In this study, the power law exponent for D, G, and P structures was estimated to be 0.32, 1.06, 1.25, and 0.45, 0.84, and 1.73, respectively, for the axial
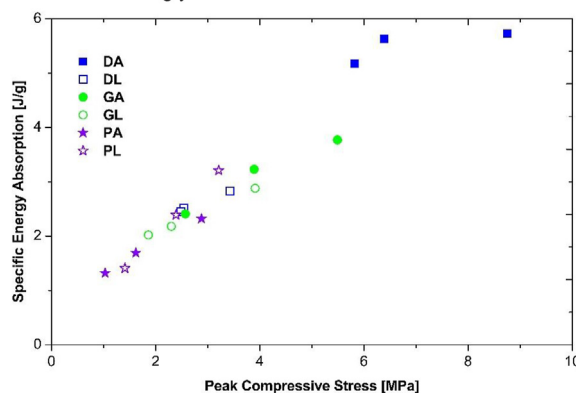

Fig. 8 — Chart representing the SEA capacity of various cell topologies concerning RD in the context of peak compressive stress.
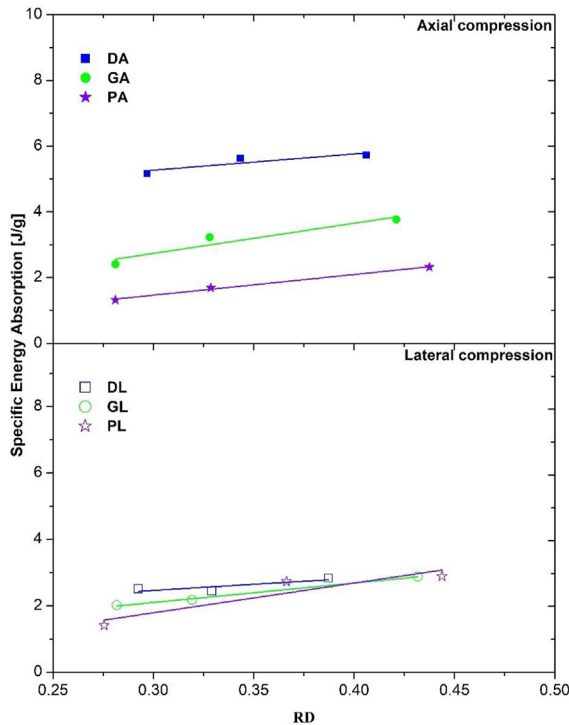
Fig. 9 — Effect of RD on SEA for various cell topologies under axial and lateral compression loading.

and lateral compressive loads shown in Fig. 9. The values of constant C and R^2 for all the fitting parameters are presented in Table 5. To list the SEA performance of the structures under axial compression, the D structure showed an average of 5.5 J/g. In contrast, the G and P structures recorded an average SEA of 3.1 J/g and 1.7 J/g, which are 43.3% and 63.8% less than the D structures, respectively. Similarly, under lateral compression, SEA was found to be 2.6 J/g, 2.36 J/g, and 2.35 J/g for the D, G, and P structures, respectively. Comparing the SEA of the structures under axial and lateral compression, an average reduction of 52.7% and 24% is observed for structures D and G, respectively, while, interestingly, an increase of 30.9% is recorded for structures P.

3.4. Deformation studies

The deformation patterns of the D, G, and P structures at different strain levels are shown in Fig. 10. Regardless of the relative density of the structures, the deformation mechanisms are primarily influenced by the cell topology. The common deformation mechanism is the stable progressive

collapse of cells horizontally layer by layer observed in all structures of this study. The deformation behavior of the structures can be better understood by analyzing the videos recorded during the experiments. In all structures, failure started within 5—10% strain, and local failures at 20% strain are observed in D structures. Layer-by-layer collapse failure under axial compression is observed in G and P structures. In G and P structures with lower RD (0.29 and 0.32), failure started in the intermediate layers and spread to the top and bottom layers, while in high-density structures (0.4), failure started in the top and bottom layers and then spread to the intermediate layers. It is observed that structures compressed parallel to the build direction (perpendicular to nozzle traverse) seldom exhibited macro cracks in D and G structures, whereas corresponding P structures displayed visible cracks generating at the circumference of a cell and propagating towards the successive cells along the interface as observed in [76]. This could be due to the induced stress concentration at the circumference of the cells of P structures due to abrupt changes in the geometry. In addition, as the interlaminar strength is comparatively lesser than the in-plane strength in the FDM process due to induced defects like porosity, wetting, and other associated manufacturing defects, cracks are likely to develop and propagate along the layer interface.

Under lateral compression, the D and G structures exhibited barreling (highlighted in black dotted lines) as shown in Fig. 11 (a), (b), with cleavage failure (highlighted in the yellow box) due to the orientation of the fibers along the loading direction leading to weak interfacial bonding, which is one of the severe limitations in FDM. Macro cracks are generated and propagated through the weakest path along the build plane of nozzle movement, as shown in Fig. 11. In addition, visible vertical cracks formed and propagated along the build plane. However, no catastrophic failures are observed as in the structures presented in [68], since the successive layers started to collapse before the complete collapse of the first layer. This is because the layers are connected along the X, Y, and Z axes.

This type of failure is influenced by the poor interfacial adhesion of the matrix and reinforcements. The P structures did not exhibit barreling but the development and propagation of vertical cracks along the plane of layer deposition through successive cells are observed. Fig. 12 shows the fiber orientation along the deposition layers of the TPMS structures in the build direction. In all D and G structures, layer collapse without the formation of shear bands or failure planes is observed. This is due to the continuous connection of the cells and the improved stress transfer through the fiber reinforcement to the successive cells, which promotes layer-by-layer collapse and eliminates local failure.

Table 5 — Gibson-Ashby power law parameters for various cell topologies compressed in axial and lateral directions.

Cell Topology	Compressive Modulus [MPa]						Compressive Peak Stress [MPa]						Specific Energy absorption [J/g]					
	Axial			Lateral			Axial			Lateral			Axial			Lateral		
	C	n	R^2	C	n	R^2	C	n	R^2	C	n	R^2	C	n	R^2	C	n	R^2
Schwarz Diamond [D]	155.89	1.54	0.88	240.1	1.56	0.82	27.82	1.31	0.94	9.57	1.12	0.81	7.75	0.32	0.83	4.27	0.45	0.71
Schoen Gyroid [G]	105	1.549	0.97	173.31	1.44	0.99	27.58	1.83	0.97	16.9	1.74	1	9.72	1.06	0.9	5.84	0.84	0.99
Schwarz Primitive [P]	63.24	1.35	0.99	124.37	1.19	0.83	19.42	2.28	0.99	13.31	1.73	0.99	6.61	1.25	0.99	13.31	1.73	0.99
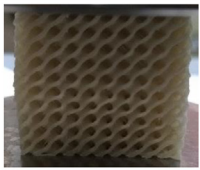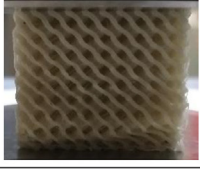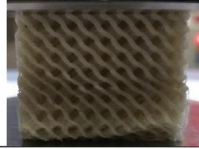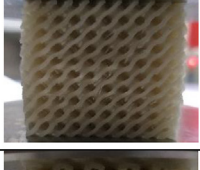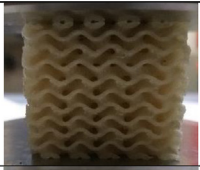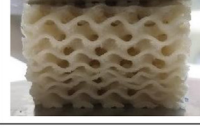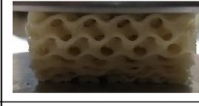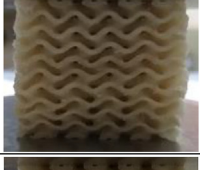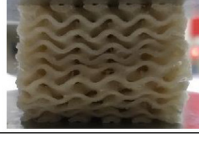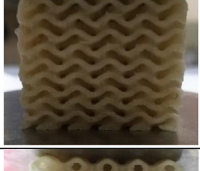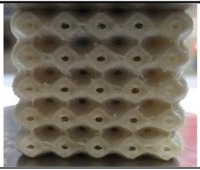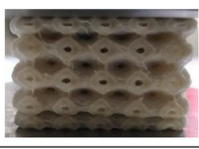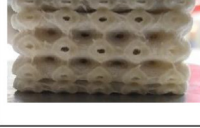
Strain (%)	RD	Є = 10	Є = 20	Є = 40	Є = 60
Schwarz Diamond	0.29				
	0.34				
	0.4				
Schoen Gyroid	0.28				
	0.32				
	0.42				
Schwarz Primitive	0.28				
	0.32				
	0.43				

Fig. 10 — Deformation in fiber-reinforced TPMS structures under axial compression.
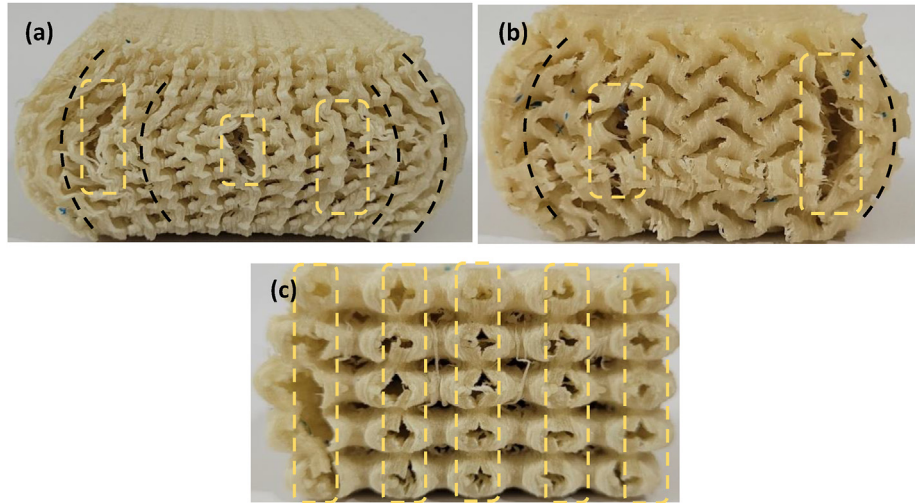
Fig. 11 — Barreling accompanied by vertical crack propagation in fiber-reinforced TPMS structures under lateral compression (perpendicular to the build direction) (a) D structure (b) G structure (c) P structure.

3.5. *Effects of short fiber reinforcement in FDM filaments*

This section summarizes the effect of short fiber reinforcement and its effects on loading direction on the TPMs structures. Through experimental observations, the compression mechanical properties of polymer structures could be significantly improved by reinforcing short glass fibers with the matrix in FDM. Compared to the literature [78], reinforced lattice structures exhibited remarkable properties in terms of energy absorption while maintaining low-stress levels under lateral compression. In addition, fiber reinforcements eliminated post-yield softening and rippling, resulting in controlled
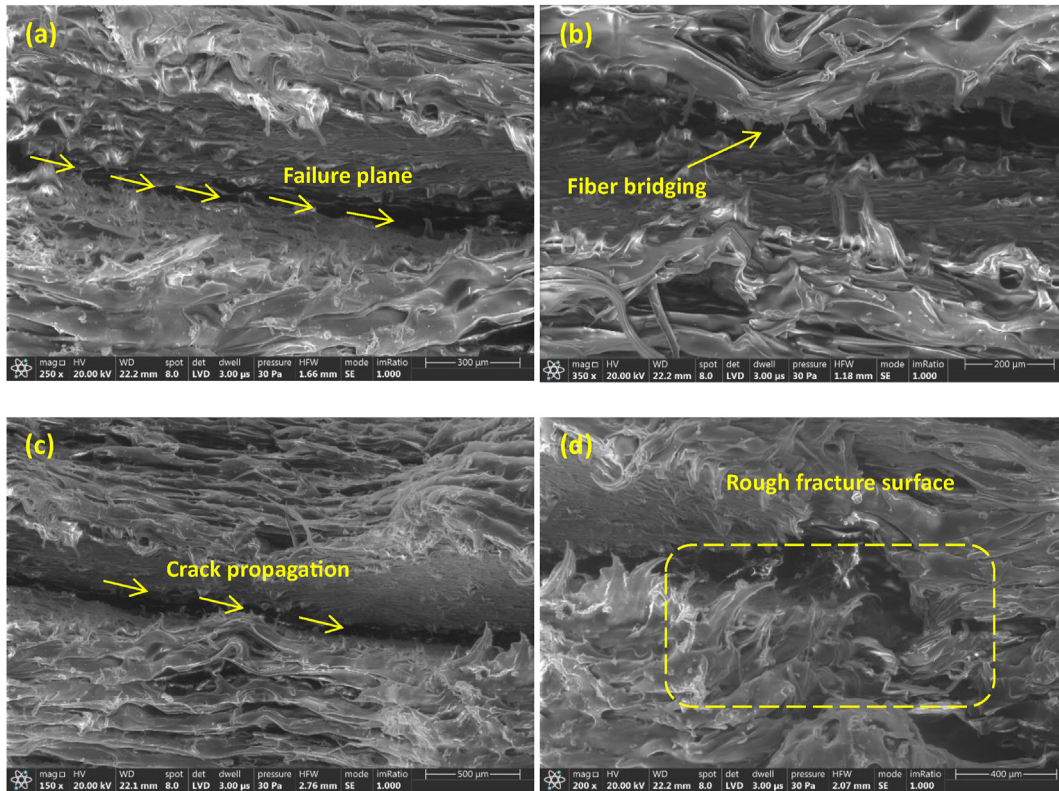
Fig. 12 — Failure morphology recorded by SEM (a) - D structure, (b) - G structure, (c, d) - P structure, (a) Failure plane in D structure along the cell boundary (b) Fiber bridging along the crack surface in G structure (c) Crack propagation along layer boundary (d) Matrix crack failure with rough fracture surface.

compressive failure. Compared to [79], the onset of densification may be extended by reinforcing short glass fibers, which offers a significant enhancement in energy absorption.

Due to the stretching failure modes observed in TPMS lattice structures, the fiber length and aspect ratio are potential parameters that could alter the compressive nature of the structures. Under axial compression, as the fibers are aligned perpendicular to the loading direction, no significant enhancement in stiffness and load-bearing properties is witnessed. This reveals that the interlaminar properties of the ductile polyamide structures are not altered by the reinforcement. However, under transverse compression, despite the stretch-dominated failure modes, all the TPMS structures suffered local bending at the weak spots where the fiber reinforcement was deficient to transfer the applied load to successive reinforcements. Following the local bending, the generation of vertical cracks was witnessed along the layer interface. However, due to the moderate fiber content in the filament (~ 25%) [65], offering enhanced overlapping of fiber reinforcements lead to better interplane bonding strength. This can be confirmed by comparing the failure behavior of unreinforced nylon P structures presented in [80].

In addition to fiber content, factors like fiber dispersion and process parameters play a significant role in the development of reliable structures with enhanced interfacial bonding [81]. The appreciable thermal conductivity of short glass fiber reinforcements promotes polymer diffusion and minimizes porosity. The SEM images presented in [54] are taken along the fracture plane showing fiber tear-out, fiber breakage, and matrix failure mechanisms in PA samples reinforced with short carbon fibers compressed in the axial direction according to ASTM D695-15 standard. Similarly, the alignment of short fibers resulted in direction-dependent material properties and significantly enhanced modulus and strength in the alignment direction [82]. In addition, rough fracture surfaces of the glass fiber-reinforced ABS parts showed improved interfacial bonding and fiber fracture accompanied by matrix cracking. These are typical crack control and failure mechanisms achieved by primary and secondary reinforcements [83,84].

4. Conclusion

Periodic TPMS cell structures with different cell topologies and relative densities are designed and fabricated by composite FDM, and subsequently, anisotropic structure-property relationships are determined using Gibson-Ashby power law in terms of compressive modulus, peak compressive stress, and specific energy absorption under axial and lateral quasi-static compression load cases. From the experimental curves, it is evident that all structures exhibited stretch-dominated compression with a progressive failure mode. This work serves as a guide in predicting the compressive mechanical properties of short fiber-reinforced TPMS structures for load-bearing applications. The key findings from this research are summarized below.

1. Schwarz Diamond exhibited appreciable printability for all relative density variations with the smallest deviations, while Schoen Gyroid structures showed negligible deviations <5% for low RD 0.28 and 0.32, but observed remarkable deviations >10% at higher RD 0.4. A similar trend was observed for Schwarz Primitive structures. All structures showed cell connectivity and layer continuity as evidenced by CT images.

2. D & G structures exhibited severe strain hardening with higher ranges of compressive stress under axial compression. In contrast, all structures showed a stable curve with a longer plateau regime with minimal slope and undulations under lateral compression. P structures exhibited stable curves with a longer plateau regime with minimal slope and undulations under both axial and lateral compression.

3. The least values of the exponent n of the power law are 1.35 and 1.19 for Schwarz primitives for the compressive modulus under axial and lateral compression. Similarly, the value of n was 2.28 and 1.73 for compressive peak stress and 1.25 and 1.73 for specific energy absorption for Schwarz Primitive under axial and lateral loading which are higher than those of D & G structures. Although loading direction had a significant effect on compressive modulus, a limited effect on maximum compressive stress and specific energy absorption is observed.

4. Under axial compression, all structures suffered a progressive layer-by-layer collapse mode of deformation rather than developing shear bands and catastrophic failure. However, under lateral compression, D and G structures barreled and all structures developed vertical cracks along the build plane and propagated towards the top and bottom edges. From the SEM images, crack propagation is witnessed along the layer boundaries.

Future work

The compression properties can be further tuned by controlling the fiber orientation, aspect ratio as well as fiber content in the filaments in conjunction with the cell topology. This would give researchers another dimension of design freedom to develop architected structures suitable for applications in diverse fields. In addition, the effects of strain rate on short fiber-reinforced bio-inspired structures are to be explored in detail.

Compliance with ethical standards

Ethics declarations

The authors declare that they have no known competing financial interests or personal relationships that could have appeared to influence the work reported in this paper.

Conflict of interest

The authors declare no conflicts of interest.

Consent to participate

All authors voluntarily agree to participate in this research study.

Consent for publication

All authors permit the Journal to publish this research study.

Availability of data and materials

All data generated or analyzed during this study are included in this published article.

Author contributions

PL and EN designed the experiment and PL, and JS performed the experimental work; PL and KM analyzed the data; PL, EN contributed to the original writing the manuscript; PL and SR contributed to review. All authors read and approved the final manuscript.

Declaration of competing interest

The authors declare that they have no known competing financial interests or personal relationships that could have appeared to influence the work reported in this paper.

REFERENCES

[1] Heinl P, Müller L, Körner C, Singer RF, Müller FA. Cellular Ti-6Al-4V structures with interconnected macro porosity for bone implants fabricated by selective electron beam melting. Acta Biomater 2008;4(5):1536–44. https://doi.org/10.1016/j.actbio.2008.03.013.

[2] Khalil M, Hassan Ali MI, Khan KA, Abu Al-Rub R. Forced convection heat transfer in heat sinks with topologies based on triply periodic minimal surfaces. Case Stud Therm Eng 2022;38:102313. https://doi.org/10.1016/j.csite.2022.102313. July.

[3] Linul E, Marşavina L, Linul PA, Kovacik J. Cryogenic and high temperature compressive properties of metal foam matrix composites. Compos Struct 2019;209:490–8. https://doi.org/10.1016/j.compstruct.2018.11.006. October 2018.

[4] Deshpande VS, Fleck NA, Ashby MF. E ective properties of the octet-truss lattice material 2001;49:1747–69.

[5] Novak JI, Novak AR. Is additive manufacturing improving performance in Sports? A systematic review. Proc Inst Mech Eng P J Sports Eng Technol 2021;235(3):163–75. https://doi.org/10.1177/1754337120971521.

[6] Surjadi JU, et al. Mechanical metamaterials and their engineering applications. Adv Eng Mater 2019;21(3):1–37. https://doi.org/10.1002/adem.201800864.

[7] Al-Ketan O, Abu Al-Rub RK. Multifunctional mechanical metamaterials based on triply periodic minimal surface lattices. Adv Eng Mater 2019;21(10). https://doi.org/10.1002/adem.201900524.

[8] Huang SH, Liu P, Mokasdar A, Hou L. Additive manufacturing and its societal impact: a literature review. Int J Adv Manuf Technol 2013;67(5–8):1191–203. https://doi.org/10.1007/s00170-012-4558-5.

[9] Thompson MK, et al. Design for additive manufacturing: trends, opportunities, considerations, and constraints. CIRP Ann - Manuf Technol 2016;65(2):737–60. https://doi.org/10.1016/j.cirp.2016.05.004.

[10] Chu C, Graf G, Rosen DW. Design for additive manufacturing of cellular structures. Comput. Aided. Des. Appl. 2008;5(5):686–96. https://doi.org/10.3722/cadaps.2008.686-696.

[11] Maconachie T, et al. The compressive behaviour of ABS gyroid lattice structures manufactured by fused deposition modelling. Int J Adv Manuf Technol 2020;107(11–12):4449–67. https://doi.org/10.1007/s00170-020-05239-4.

[12] Kadkhodapour J, Montazerian H, Raeisi S. Investigating internal architecture effect in plastic deformation and failure for TPMS-based scaffolds using simulation methods and experimental procedure. Mater Sci Eng C 2014;43:587–97. https://doi.org/10.1016/j.msec.2014.07.047.

[13] Almesmari A, Sheikh-Ahmad J, Jarrar F, Bojanampati S. Optimizing the specific mechanical properties of lattice structures fabricated by material extrusion additive manufacturing. J Mater Res Technol 2023;22:1821–38. https://doi.org/10.1016/j.jmrt.2022.12.024.

[14] Liu J, Kannan R, Zhang D, Liu T, Nandwana P, Devaraj A. Jo ur n Pr pr oo. Addit Manuf 2022:102834. https://doi.org/10.1016/j.addma.2022.102834.

[15] Cao X, et al. Mechanical performance and defect analysis of the imperfect micro smooth gyroid cylinder shell structure. June 2021;vol. 273:1–9. https://doi.org/10.1016/j.compstruct.2021.114320.

[16] Al-Ketan O, Rowshan R, Abu Al-Rub RK. Topology-mechanical property relationship of 3D printed strut, skeletal, and sheet based periodic metallic cellular materials. Addit Manuf 2018;19:167–83. https://doi.org/10.1016/j.addma.2017.12.006.

[17] Lazar PJL, Subramanian J, Manickam M, Selvaraj VK. Imperfections and computational modeling of lattice structures developed through powder bed fusion - a short review. Mater Today Proc 2023:2–7. https://doi.org/10.1016/j.matpr.2023.02.269.

[18] Sadeghi F, Baniassadi M, Shahidi A, Baghani M. TPMS metamaterial structures based on shape memory polymers: mechanical, thermal and thermomechanical assessment. J Mater Res Technol 2023;23:3726–43. https://doi.org/10.1016/j.jmrt.2023.02.014.

[19] Alizadeh-osgouei M, Li Y, Vahid A, Ataee A, Wen C. Smart Materials in Medicine High strength porous PLA gyroid scaffolds manufactured via fused deposition modeling for tissue-engineering applications. Smart Mater. Med. 2021;2:15–25. https://doi.org/10.1016/j.smaim.2020.10.003. August 2020.

[20] Al Rifaie M, Mian A. Compression behavior of three-dimensional printed polymer lattice structures 2018;0(0):1—11. https://doi.org/10.1177/1464420718770475.

[21] Pecorini G, Braccini S, Parrini G, Chiellini F. Additive manufacturing of poly (3-hydroxybutyrate- co -3-hydroxyvalerate)/poly (D , L-lactide- co -glycolide) biphasic scaffolds for bone tissue regeneration. 2022.

[22] Abueidda DW, Elhebeary M, Shiang CA, Pang S, Al-rub RKA, Jasiuk IM. Mechanical properties of 3D printed polymeric Gyroid cellular structures : experimental and fi nite element study. Mater Des 2019;165:107597. https://doi.org/10.1016/j.matdes.2019.107597.

[23] Shanmugam V, et al. Fatigue behaviour of FDM-3D printed polymers , polymeric composites and architected cellular materials. Int J Fatig 2021;143:106007. https://doi.org/10.1016/j.ijfatigue.2020.106007. August 2020.

[24] Basurto-vázquez O, Sánchez-rodríguez EP, Mcshane GJ, Medina DI. Load distribution on PET-G 3D prints of honeycomb cellular structures under compression load 2021:1—13.

[25] Bates SRG, Farrow IR, Trask RS. 3D printed polyurethane honeycombs for repeated tailored energy absorption. JMADE 2016;112:172—83. https://doi.org/10.1016/j.matdes.2016.08.062.

[26] Voyiadjis GZ, Znemah RA, Wood P. Microstructure and geometry effects on the compressive behavior of LPBF-manufactured inconel 718 honeycomb structures. J Mater Res Technol 2023;24:1562—78. https://doi.org/10.1016/j.jmrt.2023.03.093.

[27] Ataee A, Li Y, Brandt M, Wen C. Ultrahigh-strength titanium gyroid scaffolds manufactured by selective laser melting (SLM) for bone implant applications. Acta Mater 2018;158:354—68. https://doi.org/10.1016/j.actamat.2018.08.005.

[28] Al-Ketan O, Rowshan R, Palazotto AN, Abu Al-Rub RK. On mechanical properties of cellular steel solids with shell-like periodic architectures fabricated by selective laser sintering. J. Eng. Mater. Technol. Trans. ASME 2019;141(2). https://doi.org/10.1115/1.4041874.

[29] Zhang B, et al. Mechanical properties of additively manufactured Al2O3 ceramic plate-lattice structures: experiments & Simulations. Compos Struct 2023;311:116792. https://doi.org/10.1016/j.compstruct.2023.116792. January.

[30] Zhang X, Zhang K, Zhang B, Li Y, He R. Additive manufacturing, quasi-static and dynamic compressive behaviours of ceramic lattice structures. J Eur Ceram Soc 2022;42(15):7102—12. https://doi.org/10.1016/j.jeurceramsoc.2022.08.018.

[31] Abueidda DW, Abu Al-Rub RK, Dalaq AS, Lee DW, Khan KA, Jasiuk I. Effective conductivities and elastic moduli of novel foams with triply periodic minimal surfaces. Mech Mater 2016;95:102—15. https://doi.org/10.1016/j.mechmat.2016.01.004.

[32] Khaderi SN, Deshpande VS, Fleck NA. The stiffness and strength of the gyroid lattice. Int J Solid Struct 2014;51(23—24):3866—77. https://doi.org/10.1016/j.ijsolstr.2014.06.024.

[33] Xiao L, Song W. Additively-manufactured functionally graded Ti-6Al-4V lattice structures with high strength under static and dynamic loading: experiments. Int J Impact Eng 2018;111:255—72. https://doi.org/10.1016/j.ijimpeng.2017.09.018. June 2017.

[34] Mieszala M, et al. Micromechanics of amorphous metal/polymer hybrid structures with 3D cellular architectures : size effects , buckling behavior , and energy absorption capability 2017:1—13. https://doi.org/10.1002/smll.201602514.

[35] Novak N, Krstulović-Opara L, Ren Z, Vesenjak M. Mechanical properties of hybrid metamaterial with auxetic chiral cellular structure and silicon filler. Compos Struct 2020;234. https://doi.org/10.1016/j.compstruct.2019.111718. November 2019.

[36] Montazerian H, Davoodi E, Asadi-Eydivand M, Kadkhodapour J, Solati-Hashjin M. Porous scaffold internal architecture design based on minimal surfaces: a compromise between permeability and elastic properties. Mater Des 2017;126:98—114. https://doi.org/10.1016/j.matdes.2017.04.009. January.

[37] Yang E, et al. Effect of geometry on the mechanical properties of Ti-6Al-4V Gyroid structures fabricated via SLM: a numerical study. Mater Des 2019;184:108165. https://doi.org/10.1016/j.matdes.2019.108165.

[38] Maskery I, Aboulkhair NT, Aremu AO, Tuck CJ, Ashcroft IA. Compressive failure modes and energy absorption in additively manufactured double gyroid lattices. Addit Manuf 2017;16:24—9. https://doi.org/10.1016/j.addma.2017.04.003.

[39] Sun ZP, Guo YB, Shim VPW. Characterisation and modeling of additively-manufactured polymeric hybrid lattice structures for energy absorption. Int J Mech Sci 2021;191:106101. https://doi.org/10.1016/j.ijmecsci.2020.106101. May 2020.

[40] Munford M, Hossain U, Ghouse S, Jeffers JRT. Prediction of anisotropic mechanical properties for lattice structures. Addit Manuf 2020;32:101041. https://doi.org/10.1016/j.addma.2020.101041. January.

[41] Gautam R, Idapalapati S, Feih S. Printing and characterisation of Kagome lattice structures by fused deposition modelling. Mater Des 2018;137:266—75. https://doi.org/10.1016/j.matdes.2017.10.022.

[42] Sun ZP, Guo YB, Shim VPW. Deformation and energy absorption characteristics of additively-manufactured polymeric lattice structures — effects of cell topology and material anisotropy. Thin-Walled Struct 2021;169(September):108420. https://doi.org/10.1016/j.tws.2021.108420.

[43] de Aquino DA, Maskery I, Longhitano GA, Jardini AL, del Conte EG. Investigation of load direction on the compressive strength of additively manufactured triply periodic minimal surface scaffolds. Int J Adv Manuf Technol 2020;109(3—4):771—9. https://doi.org/10.1007/s00170-020-05706-y.

[44] Mohammadizadeh M, Imeri A, Fidan I, Elkelany M. 3D printed fiber reinforced polymer composites - structural analysis. Compos B Eng 2019;175(April):107112. https://doi.org/10.1016/j.compositesb.2019.107112.

[45] Mohan KHR, et al. Influence of short glass fibre reinforcement on mechanical properties of 3D printed ABS-based polymer composites. Polymers 2022;14:6. https://doi.org/10.3390/polym14061182.

[46] Chicos LA, et al. Fused filament fabrication of short glass fiber-reinforced polylactic acid composites: infill density influence on mechanical and thermal properties. Polymers 2022;14:22. https://doi.org/10.3390/polym14224988.

[47] Wang P, et al. Preparation of short CF/GF reinforced PEEK composite filaments and their comprehensive properties evaluation for FDM-3D printing. Compos B Eng 2020;198(January):108175. https://doi.org/10.1016/j.compositesb.2020.108175.

[48] Wang K, et al. Effects of printing direction on quasi-static and dynamic compressive behavior of 3D printed short fiber reinforced polyamide-based composites. Polym Adv Technol 2022;33(8):2404—15. https://doi.org/10.1002/pat.5696.

[49] Tekinalp HL, et al. Highly oriented carbon fiber — polymer composites via additive manufacturing. Compos Sci Technol 2014;105:144—50. https://doi.org/10.1016/j.compscitech.2014.10.009.

[50] K. Wang, S. Li, Y. Rao, Y. Wu, Y. Peng, and S. Yao, "Flexure behaviors of ABS-based composites containing carbon and kevlar fibers by material extrusion 3D printing," pp. 1—12.

[51] Liao G, et al. Properties of oriented carbon fiber/polyamide 12 composite parts fabricated by fused deposition modeling. Mater Des 2018;139:283—92. https://doi.org/10.1016/j.matdes.2017.11.027.

[52] Ning F, Cong W, Hu Z, Huang K. Additive manufacturing of thermoplastic matrix composites using fused deposition modeling: a comparison of two reinforcements. J Compos Mater 2017;51(27):3733—42. https://doi.org/10.1177/0021998317692659.

[53] Ning F, Cong W, Hu Y, Wang H. Additive manufacturing of carbon fiber-reinforced plastic composites using fused deposition modeling: effects of process parameters on tensile properties. J Compos Mater 2017;51(4):451—62. https://doi.org/10.1177/0021998316646169.

[54] Wang J, et al. Effects of scanning strategy and printing temperature on the compressive behaviors of 3D printed polyamide-based composites. Polymers 2020;12(no. 8). https://doi.org/10.3390/polym12081783.

[55] Gibson LJ, Ashby MF. The mechanics of foams: refinements. 2014 [Chapter 3].

[56] Yan C, Hao L, Hussein A, Young P, Huang J, Zhu W. Microstructure and mechanical properties of aluminium alloy cellular lattice structures manufactured by direct metal laser sintering. Mater Sci Eng, A 2015;628:238—46. https://doi.org/10.1016/j.msea.2015.01.063.

[57] Dalaq AS, Abueidda DW, Abu Al-Rub RK. Mechanical properties of 3D printed interpenetrating phase composites with novel architectured 3D solid-sheet reinforcements. Composer Part A Appl Sci Manuf 2016;84:266—80. https://doi.org/10.1016/j.compositesa.2016.02.009.

[58] Zhou H, et al. Lightweight structure of a phase-change thermal controller based on lattice cells manufactured by SLM. Chin J Aeronaut 2019;32(7):1727—32. https://doi.org/10.1016/j.cja.2018.08.017.

[59] Jung Y, Chu KT, Torquato S. A variational level set approach for surface area minimization of triply-periodic surfaces. J Comput Phys 2007;223(2):711—30. https://doi.org/10.1016/j.jcp.2006.10.007.

[60] Abou-ali AM, Al-ketan O, Lee D, Rowshan R, Al-rub RKA. Mechanical behavior of polymeric selective laser sintered ligament and sheet based lattices of triply periodic minimal surface architectures. Mater Des 2020;196:109100. https://doi.org/10.1016/j.matdes.2020.109100.

[61] Hsieh M, Valdevit L. Minisurf — a minimal surface generator for finite element modeling and additive manufacturing. Softw. Impacts 2020;6:100026. https://doi.org/10.1016/j.simpa.2020.100026. July,.

[62] Peng C, Tran P, Mouritz AP. Compression and buckling analysis of 3D printed carbon fibre-reinforced polymer cellular composite structures. Compos Struct 2022;300(August):116167. https://doi.org/10.1016/j.compstruct.2022.116167.

[63] Abou-Ali AM, Al-Ketan O, Lee DW, Rowshan R, Abu Al-Rub RK. Mechanical behavior of polymeric selective laser sintered ligament and sheet based lattices of triply periodic minimal surface architectures. Mater Des 2020;196:109100. https://doi.org/10.1016/j.matdes.2020.109100.

[64] Ahn SH, Montero M, Odell D, Roundy S, Wright PK. Anisotropic material properties of fused deposition modeling ABS. Rapid Prototyp J 2002;8(4):248—57. https://doi.org/10.1108/13552540210441166.

[65] https://www.esun3d.com/uploads/eSUN_ePA-GF-Filament_TDS_V4.0.pdf.

[66] Mohamed OA, Masood SH, Bhowmik JL. Optimization of fused deposition modeling process parameters: a review of current research and future prospects. Adv Manuf 2015;3(1):42—53. https://doi.org/10.1007/s40436-014-0097-7.

[67] Jiang J, Ma Y. Path planning strategies to optimize accuracy, quality, build time and material use in additive manufacturing: a review. Micromachines 2020;11:7. https://doi.org/10.3390/MI11070633.

[68] Maconachie T, et al. The compressive behaviour of ABS gyroid lattice structures manufactured by fused deposition modelling. 2020. p. 4449—67.

[69] Ma Z, Zhang DZ, Liu F, Jiang J, Zhao M, Zhang T. Lattice structures of Cu-Cr-Zr copper alloy by selective laser melting: microstructures, mechanical properties and energy absorption. Mater Des 2020;187:108406. https://doi.org/10.1016/j.matdes.2019.108406.

[70] Liang Y, et al. Energy absorption and deformation behavior of 3D printed triply periodic minimal surface stainless steel cellular structures under compression. Steel Res Int 2021;92(3). https://doi.org/10.1002/srin.202000411.

[71] Liu Y, Schaedler TA, Jacobsen AJ, Chen X. Quasi-static energy absorption of hollow microlattice structures. Compos B Eng 2014;67:39—49. https://doi.org/10.1016/j.compositesb.2014.06.024.

[72] Liu X, Suzuki A, Takata N, Kobashi M, Kato M. Dual plateau stress of C15-type topologically close-packed lattice structures additive-manufactured by laser powder bed fusion. Scripta Mater 2021;202:114003. https://doi.org/10.1016/j.scriptamat.2021.114003.

[73] Arvieu C, Galy C, Le Guen E, Lacoste E. Relative density of SLM-produced aluminum alloy parts: interpretation of results. J. Manuf. Mater. Process. 2020;4(3). https://doi.org/10.3390/JMMP4030083.

[74] Wang X, Jiang M, Zhou Z, Gou J, Hui D. 3D printing of polymer matrix composites: a review and prospective. Compos B Eng 2017;110:442—58. https://doi.org/10.1016/j.compositesb.2016.11.034.

[75] Zhang C, et al. Mechanical characteristics and deformation mechanism of functionally graded triply periodic minimal surface structures fabricated using stereolithography. Int J Mech Sci 2021;208:106679. https://doi.org/10.1016/j.ijmecsci.2021.106679. July.

[76] Yu S, Sun J, Bai J. Investigation of functionally graded TPMS structures fabricated by additive manufacturing. Mater Des 2019;182:108021. https://doi.org/10.1016/j.matdes.2019.108021.

[77] Saleh M, Anwar S, Al-Ahmari AM, Alfaify A. Compression performance and failure analysis of 3D-printed carbon fiber/PLA composite TPMS lattice structures. Polymers 2022;14:21. https://doi.org/10.3390/polym14214595.

[78] Higuera S, Miralbes R, Ranz D. Mechanical properties and energy—absorption capabilities of thermoplastic sheet gyroid structures. Mech Adv Mater Struct 2022;29(25):4110—24. https://doi.org/10.1080/15376494.2021.1919803.

[79] Miralbes R, Ranz D, Pascual FJ, Zouzias D, Maza M. Characterization of additively manufactured triply periodic minimal surface structures under compressive loading. Mech Adv Mater Struct 2022;29(13):1841—55. https://doi.org/10.1080/15376494.2020.1842948.

[80] Maskery I, et al. Insights into the mechanical properties of several triply periodic minimal surface lattice structures made by polymer additive manufacturing. Polymer 2018;152:62—71. https://doi.org/10.1016/j.polymer.2017.11.049.

[81] Coogan TJ, Kazmer DO. Modeling of interlayer contact and contact pressure during fused filament fabrication. J Rheol (N Y, NY, U S) 2019;63(4):655—72. https://doi.org/10.1122/1.5093033.

[82] Wright WJ, Koerner H, Rapking D, Abbott A, Celik E. Rapid fiber alignment quantification in direct write printing of short fiber reinforced composites. Compos B Eng 2022;236:109814. https://doi.org/10.1016/j.compositesb.2022.109814. March.

[83] Lazar PJL, Sengottuvelu R, Natarajan E. Assessments of secondary reinforcement of epoxy matrix-glass fibre composite laminates through nanosilica (SiO2). Materials 2018;11:11. https://doi.org/10.3390/ma11112186.

[84] Prince Jeya Lal L, Ramesh S, Parasuraman S, Natarajan E, Elamvazuthi I. Compression after impact behaviour and failure analysis of nanosilica-toughened thin epoxy/gfrp composite laminates. Materials 2019;12:19. https://doi.org/10.3390/ma12193057.